Numerical framework for multi-scale modeling planar DC magnetron sputtering

Si Bui Quang Tran [a]*, Fong Yew Leong [a], Ramanarayan Hariharaputran [a], Ding Wenjun [a], Po-Yen Lai [a], Duc Vinh Le [a]

[a] *Institute of High Performance Computing (IHPC), Agency for Science, Technology and Research (A*STAR), 1 Fusionopolis Way, Connexis, Singapore 138634, Republic of Singapore.*

*Corresponding author.

E-mail address: transbq@ihpc.a-star.edu.sg (SBQ Tran).

ABSTRACT

In this study, we propose a numerical framework for multi-scale modeling planar Direct Current (DC) magnetron sputtering for a single alloy target. In the model, we account for electromagnetics, fluid dynamics, discharge chemistry and thermal transport across multiple length scales. Specifically, we employ Lattice Boltzmann Method (LBM) for transport phenomena, Finite Elements Method (FEM) for magnetron discharge transport, and binary collision approximation Monte-Carlo method for sputtering and atomic deposition. Our modeling framework could predict the composition, uniformity, and deposition flux of deposited thin film alloys. Furthermore, the simulation also provides the information of plasma in the chamber such as electron, ion densities, argon ion energy and argon ion flux bombarding on the target. Through parametric analyses, we found that substrate film composition is scaled with both chamber pressure and inverse chamber temperature, although the effect of chamber temperature is considerably marginal under low pressure conditions. We also found that magnetic fields do not influence the film composition, but it significantly affects the substrate deposition flux and film uniformity. Our work provides useful insights to operational heuristics involved in magnetron sputtering and other physical chemical processes.

Keywords: planar DC magnetron sputtering, composition, thin film, discharge, rarefied gas

1. Introduction

Sputter deposition is an important technology widely employed in thin film deposition [1, 2]. In a discharge chamber, the sputtering process is initiated by the bombardment of discharge ions to a solid target [3, 4], which knocks out atoms from a "target" source to be deposited on a "substrate", typically a silicon wafer. A typical planar magnetron sputtering setup [5] includes two concentric permanent magnets with different pole direction located near the target and outside the chamber. The magnetic fields generated by the magnets confine electrons through the Lorentz force, such that the electrons migrate in a helical shape trajectory revolving around the chamber axis [6]. In magnetron sputtering, the composition, substrate deposition flux and uniformity in coating process are important factors for ensuring consistent quality and physical characteristics of thin films.

Planar DC magnetron sputtering is a complex multiscale operation. To simulate gas discharge, there exist hybrid fluid models for ions and slow electrons coupled with Monte Carlo method for fast electrons [7], and for ions coupled with particle-in-cell/Monte Carlo method for electrons [8, 9]. Although the fluid model is computationally efficient, it is less accurate under rarefied conditions where the mean free path of charged particles exceed the characteristic length of the discharge. Hence, the drift-diffusion approximation may not be valid under low working gas pressures, even though local collisions may be enhanced by focusing of electrons near the cathode [10].

Computational methods such as Molecular Dynamics (MD) [11-14] are widely used to simulate sputtering processes on target and deposition process of sputtered atom on substrate. Shaginyan *et al.* [15] conducted Direct Monte-Carlo (DMC) simulations of gas-phase transport of sputtered species to study the mechanism of the film composition formation during magnetron sputtering of W-Ti. The Monte-Carlo method using binary-collision approximation is computationally economical for simulating sputtering processes and an exemplary open software package for this is the 'The Stopping and Range of Ions in Matter' (SRIM) [16]. The companion software packages, TRIDYN [17] and SDTrimSP [18, 19], cater to other aspects of dynamic simulations, and they are demonstrably successful in describing collision effects in solids. Independently, Depla *et al* [20, 21] developed the software SIMTRA which employs the binary-collision approximation Monte-Carlo method to simulate the transportation of sputtered atoms from target to deposit on substrate in the rarefied gas environment. The software is freely available for download in a compiled version.

Here, we briefly review the use of software packages on sputtering models. Using TRIDYN and SIMTRA, Achenbach *et al.* [22] studied the angle-resolved composition evolution of Mo-B-C thin films deposited from a Mo_2BC compound target. Using SRIM and SIMTRA, Aeken *et al.* [20] studied the metal flux from a rotating cylindrical magnetron and Mares *et al.* [23] the effects of energetic particles on pulsed magnetron sputtering of hard nanocrystalline MBCN (M=Ti, Zr, Hf) films. Using RSD2013, SIMTRA and SRIM, Strijckmans *et al.* [24] simulated target erosion during reactive sputtering. Rezek *et al.* [25] coupled a reactive high-power impulse magnetron sputtering model and discharge model for the ionization region to study the role of discharge parameters on WO_x composition and deposition rate. These numerical studies are not self-contained, often requiring external inputs such as the experimental discharge current and target erosive profiles.

In this present work, we propose a unified sequential one-way coupled model for steady state planar magnetron sputtering. First, the fluid flow and heat transfer in rarefied gas in the discharge chamber are simulated using Lattice Boltzmann Method (LBM). The resultant velocity, pressure and temperature distributions are inputs for the magnetron discharge simulation using Finite Element Method (FEM) to determine the flux, velocity, and spatial distribution of argon ions on the surface of the target. Using SDTrimSP, we determine the sputtering yield for each metal species on the alloy target. These sputtering yields and the argon ion flux distribution on the target serve as inputs for solving the transport of sputtered atoms onto the substrate using SIMTRA. Our model yields useful results for applications, specifically (1) the composition of thin film, (2) film uniformity, and (3) the sputtering deposition flux on the substrate.

This paper is organized as follows. Details of the numerical methodology is described in **Section 2**. The numerical result is provided in **Section 3**. Finally, results and discussion are summarized in **Section 4**.

2. Methodology

2.1. Process flow

Magnetron sputtering is a complex physical process coupled across length and time scales. In our modeling approach, we list individual sub-process steps and solve each step sequentially. **Fig. 1** shows the flow chart for steady state simulation of magnetron sputtering with Al-Sc alloy target in argon gas discharge chamber. The overall process can be considered as one-way coupled because each sequential step does not affect the preceding one.

To simulate magnetron DC discharge, we solve for heat transfer and rarefied gas flow in the chamber which yields velocity (v) and temperature (T) distributions as inputs for the subsequent discharge simulation. We assume that discharge does not increase the gas temperature, as the pressure in the chamber is quite low and only a small part of neutral argon gas is ionized. The electron density is on the order of $10^{16}/m^3$, compared to the neutral argon gas density on the order of $10^{20}/m^3$. Electrons are heated, but due to the low electron density, the overall gas temperature is not significantly affected by either cold or non-equilibrium discharges.

For rarefied gases under low pressures, the Lattice Boltzmann Method (LBM) is an appropriate method to solve the flow field and temperature distribution in the chamber [26]. Here, we solve the Boltzmann equation for thermal flow fields in a rarefied argon gas chamber and implement our in-house developed Multiple Relaxation Time Lattice Boltzmann Method [27, 28] code for the solution of heat and rarefied gas transport.

In the present work, we employ the fluid model [10, 29], which describes the discharge in terms of macroscopic quantities by assuming a specific form of the distribution function and taking velocity moments of the Boltzmann equation. The set of coupled partial differential equations are solved using the Finite Elements Method (FEM) implemented on COMSOL Multiphysics version 5.6 [30] with Plasma module. The electron density and the electron energy are solved using drift diffusion approximation and the motion of argon ions is modeled using a simplified form of Maxwell-Stefan equations. Details of the fluid model for planar DC magnetron discharge, plasma chemical reaction and their collision cross-sections can be found in the **Appendix A**.

In the discharge simulation, argon ions impact on the target with flux (Γ_{Ar^+}) at an incident angle (θ_{Ar^+}). Under low pressure conditions, the electrophoretic ion velocity $v = \mu E$, where μ is the ion mobility and E is the electric field, is not valid if the mean free path equals to or exceeds the characteristic thickness of the discharge sheath. To calculate the argon ion velocity, we conduct particle tracking simulation separately to solve for charged particle trajectories. Initial charged particle positions in the chamber follow the argon ion density distribution obtained from discharge simulation. Accelerated by electric (E) and magnetic (B) fields, the charged ion mobility follows $dv/dt = [q(E + v \times B) + F_{col}]/m_{Ar^+}$, where F_{col} is the elastic collision and resonant charge exchange reaction force between an argon ion and a background neutral argon atom.

The information of the flux (Γ_{Ar+}), kinetic energy (E_{Ar+}) and incident angle (θ_{Ar+}) serves as inputs to calculate yield factor for each metal in the alloy target such as Aluminum (Al)-Scandium (Sc) using SDTrimSP, a Monte Carlo program designed for atomic collisions in amorphous targets using binary collision approximation. It calculates ranges, reflection coefficients and sputtering yields as well as more detailed information like depth distributions of implanted and energy distributions of backscattered and sputtered atoms.

The knocked-out atomic fluxes of each metal (Γ_{Al}, Γ_{Sc}) are computed by multiplying the respective sputtering yield and incident argon ion flux. Sputtered atoms are then transported to the substrate through rarefied gas and this process is simulated by SIMTRA software based on binary collision approximation Monte-Carlo method. Finally, the deposition flux of each metal (r_{Al}, r_{Sc}) onto the substrate are calculated, yielding the composition of the thin film.

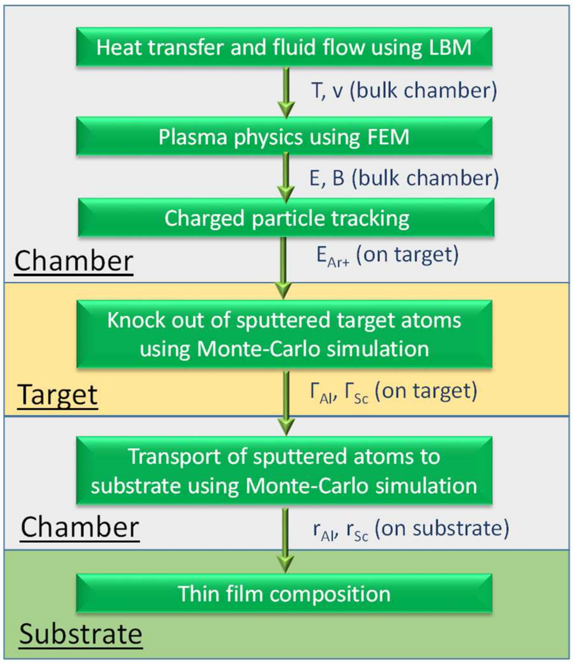

Fig. 1. Process flow chart for DC magnetron sputtering simulation.

2.2 Strengths and limitations

The advantages of the fluid model are that it can efficiently solve the transport and chemical reaction equations and couple plasma and the electromagnetic fields. Our numerical methodology has several advantages over one that relies on SIMTRA and SRIM only, such as Ref. [31]. First, a SIMTRA–SRIM model requires additional experimental input such as discharge current and target erosive racetrack. Second, to compute the sputtering yield, SIMTRA–SRIM model requires knowledge of the argon ion energy, which is difficult to measure experimentally. Third, our method resolves the spatial distributions of argon ion flux and sputtering yield on the target surface, whereas SIMTRA–SRIM model is limited to the aggregate argon ion flux and the average value of sputtering yield.

Although the fluid model is computationally efficient, the drift-diffusion approximation may not be valid under rarefied conditions, where the mean free path of charged particles exceed the characteristic length of the discharge. Also, gas rarefaction due to gas heating, sputtering and kick-out of the working gas atoms from cathode are not considered in SIMTRA. Despite these limitations, our proposed approach is able to simulate thin film compositions which compare favorably with experimental measurements (see **Section 3.1.3**).

2.3 Model validation

We compare and validate discharge simulation and SIMTRA calculations with Costin [10] and Swann [32]. Using a fluid model, Costin *et al.* [10] modeled two-dimensional axisymmetric discharge in cylinder chamber with radius and height of 26.95 mm contains argon gas at temperature of 350 K and pressure of 20 mTorr. The cathode with radius of 16.5 mm is applied a constant voltage of -550 V. The side and upper walls of chamber are grounded. The concentric magnets below the cathode generate a magnetic field with strength of 750 G on the cathode surface at the radial location of 9.5 mm. Our simulated electron density concentrates as a spotlight near the cathode at the radial location of 9.35 mm (**Fig. 2a**). Both the electron density (n_e) and argon ion density (n_i) along the z-direction at radial location of 9.35mm are in qualitative agreement with Costin's work [10] (**Fig. 2b**). The maximum electron and argon ion densities are about 2.5x10^{16}m^{-3} at z-location of 5 mm.

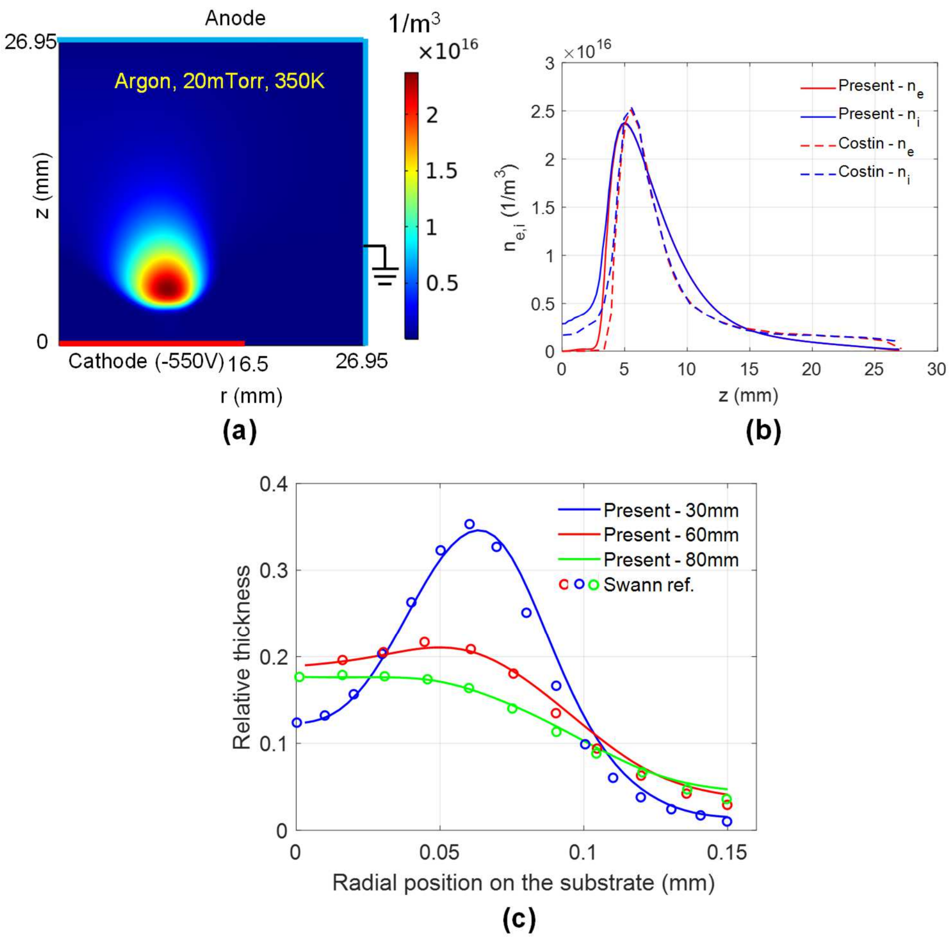

Fig. 2. (a) Chamber dimension, discharge operating conditions and our simulated electron density distribution in the computational domain [10]. (b) Electron density (n_e) and argon ion density (n_i) along the z direction at radial position r=9.35 mm vs Costlin et al. [10]. (c) Comparison of relative film thickness for target-substrate distance of 30, 60, 80 mm cases between present SIMTRA simulation and Swann's analytical calculations [32].

Swann [32] derived an analytical solution for deposited thin film thickness in a planar magnetron geometry containing two parallel circular disks of target and substrate. We simulated chamber pressure 0.4 Pa, copper target, target circular radius 100 mm, substrate circular radius 150 mm, using available target erosion data in the reference for three target-substrate distances of 30, 60, 80 mm. Based on SIMTRA calculations, our relative film thicknesses for target-substrate distance of 30, 60, 80 mm cases are in good agreement with Swann's analytical calculations [32] especially near the center (**Fig. 2c**).

2.4 Geometry setup

We model an idealized two-dimensional axisymmetric magnetron sputtering discharge cylindrical chamber (**Fig. 3**) with radius 0.1 m, height 0.05 m filled with 0.67 Pa argon gas with designated inlet and outlet vents. The circular substrate plate with radius 0.025 m is heated up to 225^{0}C. Two concentric permanent magnets with opposite magnetic polarities are located above a circular target plate with radius 0.05 m. The radius of magnets center (r_m) is 0.0225 m. The magnetic sources are modeled as boundary conditions as the magnets located non-intrusively within the chamber outside the model domain. For DC magnetron, the substrate is grounded, and the target is held at a negative potential of -270 V on a RC circuit to limit the discharge current.

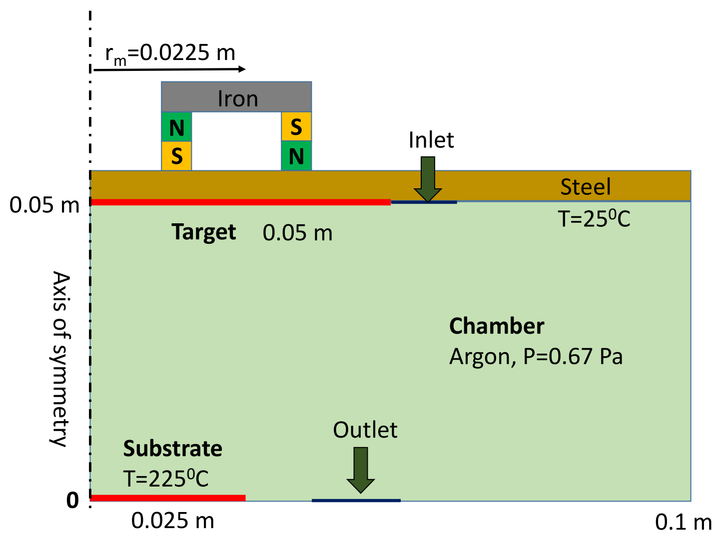

Fig. 3. Computational domain for an idealized two-dimensional axisymmetric magnetron sputtering discharge chamber.

3. Result and discussion

3.1 Magnetron sputtering of Al-Sc alloy

We present results for magnetron sputtering discharge set up according to **Fig. 3** for Al-Sc alloy, in terms of field solutions, particle transport and film composition.

3.1.1 Electromagnetics, thermal and flow fields

Fig. 4a and b shows the velocity magnitude of argon flow obtained from an LBM simulation using our in-house code with an applied inlet velocity boundary condition of 0.06 m/s, and the temperature distribution in the chamber, to be used as the inputs for discharge simulation. **Fig. 4c** shows the magnetic field lines and the region where electrons are concentrated by the Lorentz force $(F_{Lorentz} = qE + qv_e \times B)$ [6]. Since the electron velocity vector is normal to the substrate surface, the magnitude of the second term of Lorentz force is at maximum when the local magnetic field line is parallel to the substrate surface denoted by point A **(Fig. 4c)**. The second term of Lorentz force vector is directed out of plane resulting in a helical electron trajectory revolving the chamber axis. **Fig. 4d** highlights the increased electron number density at the region around point A **(Fig. 4c)**. Resolved components of electromagnetic fields are provided in **Appendix B**.

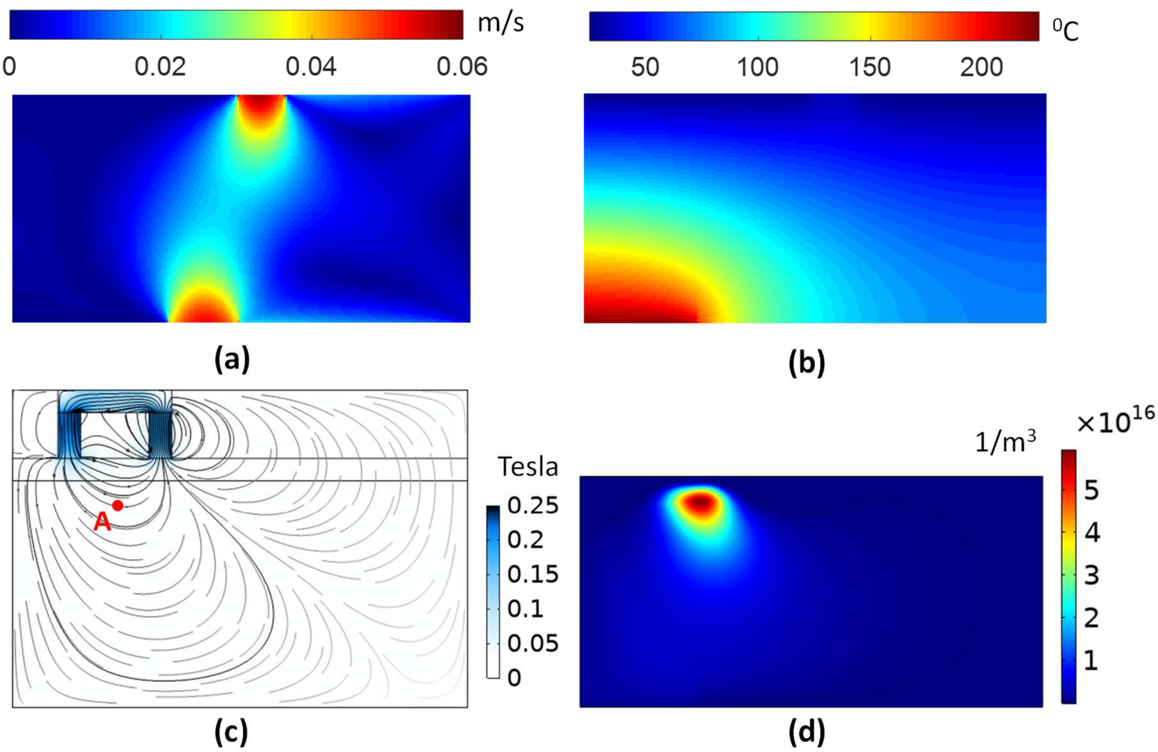

Fig. 4. (a) Velocity magnitude of flow field (LBM). (b) Temperature distribution (LBM). (c) Magnetic field magnitude and magnetic field streamline (FEM). (d) Discharge electron density distribution (FEM).

3.1.2 Particle transport

Fig. 5 shows solution snapshots of argon ion distributions and velocities in the chamber taken at times 1, 5, 20 and 50 μs based on the separated charged particle tracking simulation. Accelerated by Lorentz forces, most argon ions migrate towards and are confined near the target, while some stick onto chamber walls. By 50 μs, all charged particles are already trapped along chamber boundaries. Additional details of argon ion energy and profile on the target are provided in **Appendix B**.

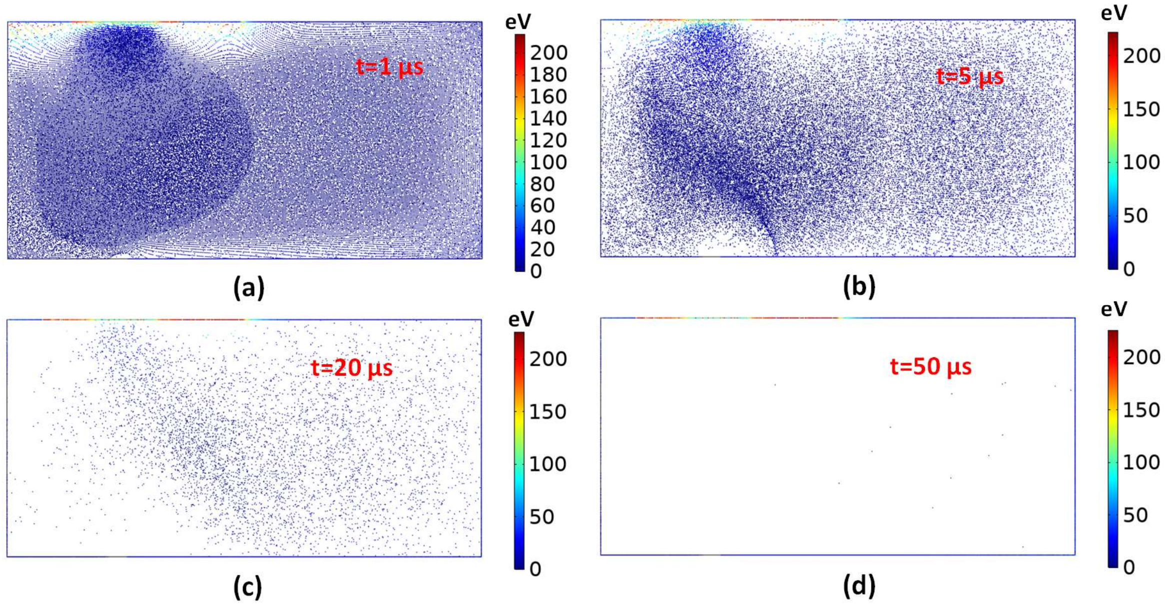

Fig. 5. Argon ion particles distribution and velocity in the chamber from charged particle tracking simulation at different time. (a) t=1 µs. (b) t=5 µs. (c) t=20 µs and (d) t=50 µs.

Fig. 6a shows the argon ion flux at the target whose alloy composition of is 60% Al and 40% Sc. **Fig. 6b** shows that the sputtering yield of Al is higher than Sc on alloy target computed using SDTrimSP. We use the heat of sublimation of each metal species as its surface binding energy [33]. For Al-Sc alloy, the surface binding energies of Al and Sc are 3.36eV and 3.49eV, respectively. Coupling the kinetic energy of argon ion (**Fig. B2b**) with sputtering yield (**Fig. 6b**), we derive the distribution of Al and Sc sputtering yields on the target (**Fig. 6c**). The sputtered atomic flux distribution of Al and Sc (**Fig. 6d**) from the target are obtained by taking products of the sputtering yields (**Fig. 6c**) and argon ion fluxes (**Fig. 6a**). More atoms are knocked out at the projection location of discharge spotlight and more Al atoms are sputtered than Sc atoms due to the higher Al mole fraction in the alloy target.

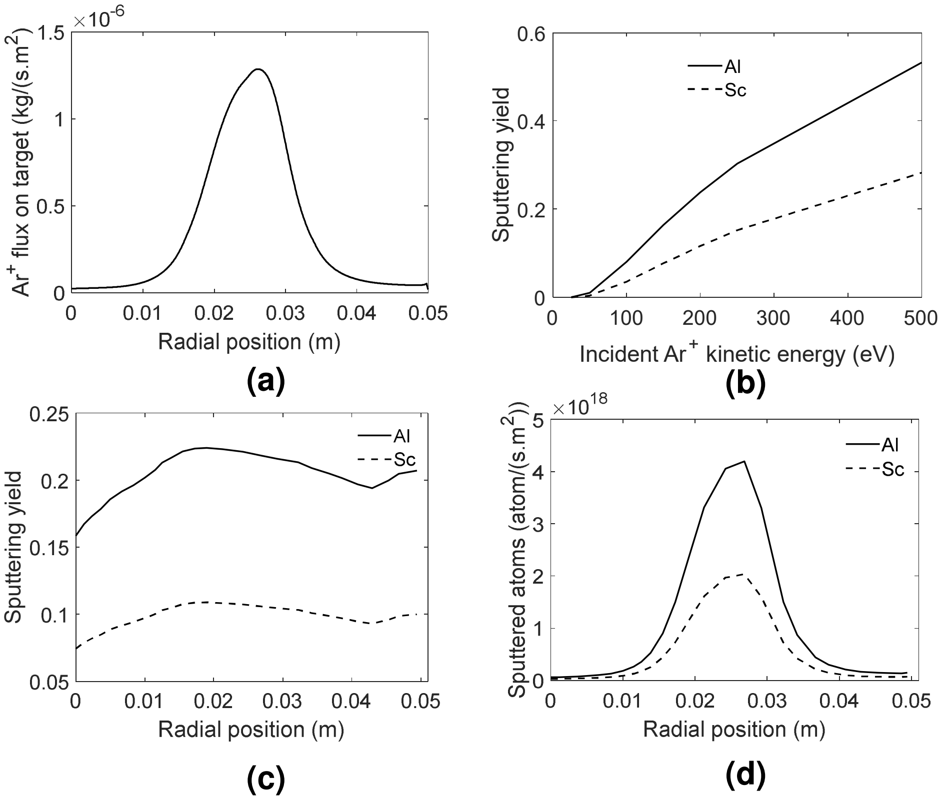

Fig. 6. On target: (a) Argon ion flux. Sputtering yields of Al and Sc as a function of (b) incident Ar ion kinetic energy based on SDTrimSP, and (c) radial distance from center. (d) Sputtered atomic distribution of Al and Sc from the target.

Sputtered atoms knocked out from the target migrate to the substrate in the rarefied gas environment. Since the number density of neutral background Ar atoms is three orders of magnitude greater than other species such as electron, argon ion and sputtered atoms, sputtered atoms are assumed to undergo elastic collision only with the neutral background gas.

Using SIMTRA, we perform independent transport simulations of sputtered Al and Sc. **Fig. 7(a, b)** shows the relative distribution of Al and Sc atoms on the substrate assuming racetrack distribution of each metal ejected from target whose energy is modeled by a Thompson distribution [34] at an angle distribution following cosine function [20]. The deposition flux of each metal (**Fig. 7c**) is obtained from the flux of sputtered and the distribution of deposited atoms on the substrate. The composition of thin film alloy based on ratio of deposition flux of each metal (**Fig. 7d**) is uniformly distributed, averaging 64.2% and 35.8% for a 60% Al and 40% Sc target, respectively.

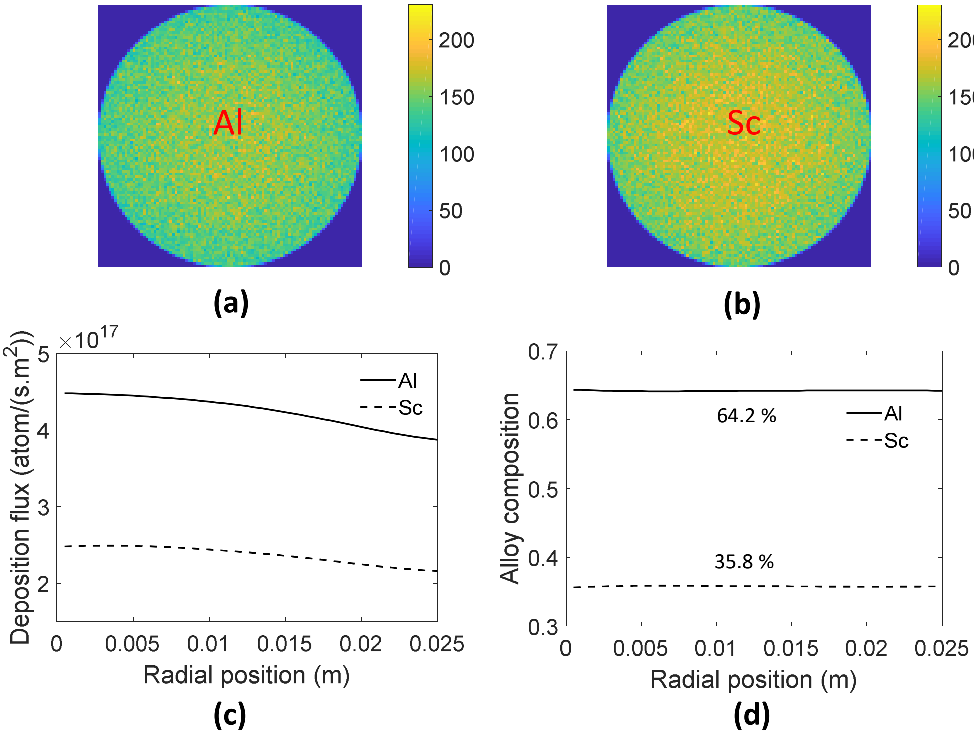

Fig. 7. On substrate: Relative (a) Al and (b) Sc atoms distributions. (c) Deposition flux of Al and Sc and (d) alloy composition of deposited thin film depending on radial distance from center.

3.1.3 Thin film composition

For purposes of validation, we simulate and compare thin film composition against experimental data found in the following references:

1. Chen *et al.* [35] fabricated Mo-Nb-Ta-V-W high entropy alloys (HEA) thin films with working pressure at 0.67 Pa, temperature at 100 ^{0}C, and input argon gas flowrate at 30 sccm. Target composition is 20% for each metal.

2. Schwarz *et al.* [36] fabricated Co-Cr-Fe-Ni High-Entropy Alloy (HEA) thin films with working pressure at 1.5 Pa and input argon gas flowrate at 50 sccm. Target composition is 30.7% Ni, 26.6% Fe, 19.7% Cr and 23% Co.

Simulations are set up according to chamber pressure and temperature, and other parameters as indicated, using magnets arrangement in Al-Sc alloy target case. **Fig. 8** shows the composition of deposited Mo-Nb-Ta-V-W and Ni-Fe-Cr-Co thin films from experiment (second column) and from the simulation (third column). The root mean square error of thin film composition between experiment and simulation is 1.18 % and 1.43 %, respectively.

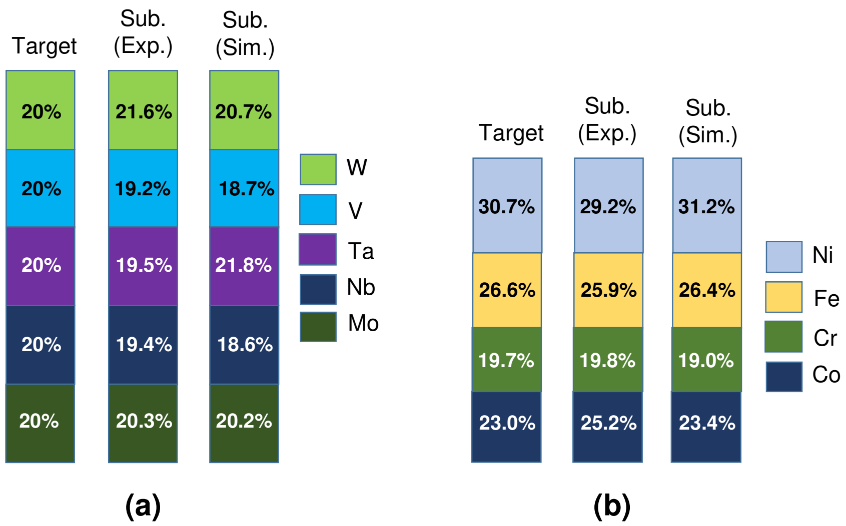

Fig. 8. Stoichiometric composition of alloy target (first column), experimentally deposited thin film on the substrate from reference (second column), and from present simulations (third column). (a) Alloy target of Mo-Nb-Ta-V-W from Ref. [35] and (b) alloy target of Ni-Fe-Cr-Co from Ref. [36].

3.2 Parametric study

We investigate the effects of geometry, discharge properties and chamber working conditions on the deposition flux, thin film uniformity and composition. Here, we confine our study to target composition of 60% Al, 40% Sc in an idealized computational domain (**Fig. 3**).

3.2.1 Chamber pressure and temperature

The chamber pressure (P) and temperature (T), taken as temperature of the argon gas, affect the composition of thin films deposited through sputtered transport. Under the SIMTRA framework, a sputtered atom navigates through gas molecules via sequence of straight trajectories and deflections from elastic collisions until deposition on a surface occurs. The mean free path of a sputtered atom relates to the probability of collision with a background gas atom, which is, in turn, inversely proportional to gas density, a function of chamber pressure and temperature as $n_g = P/(k_B T)$.

Fig. 9 shows how the Sc content (percentage by number of atoms) in the deposited thin film on the substrate depends on chamber temperature and pressure. Generally, higher Sc content can be achieved at higher pressure and lower temperature. Under low pressures (e.g. P < 0.25 Pa), we observe that Sc content is relatively insensitive to changes in the temperature, compared to under high pressure conditions (e.g. P > 2 Pa), where the Sc content is shown to scale linearly with pressure and inverse temperature parameters $\Delta Sc \sim P/T$.

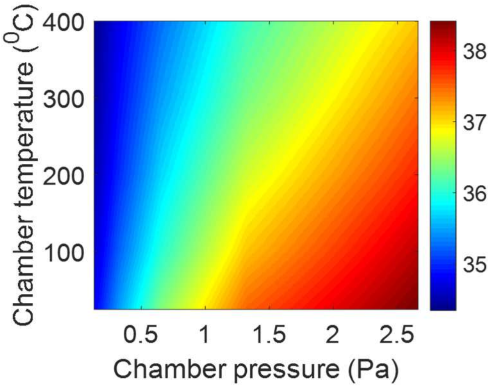

Fig. 9. Color map of Sc content (% at) in thin film on substrate depends on chamber temperature (°C) and pressure (Pa).

At gas pressures lower than 0.25 Pa, the deposition fluxes of Sc and Al are relatively insensitive to the temperature. Increasing pressure or decreasing chamber temperature effectively reduces the mean free path or augmenting the number of collisions. During an elastic collision, the kinetic energy of sputtered atom is transferred to neutral argon gas atoms and heavier atoms lose more energy than lighter ones [37]. Since the scattering angle is proportional to the sputtered atoms energy [20], heavier sputtered atoms (Sc) scatter less than the lighter ones (Al) on collision. For example, the average scattering angle for Al and Sc are 0.89 and 0.75 radians respectively at P = 2 Pa and T = 400 K.

3.2.2. Magnetic field

Fig. 10a shows how the Ar^+ ionic flux on the target surface depends on the magnitude of permanent magnets remanence or residual magnetism B = {0.15, 0.20, 0.25, 0.30} T. As expected, the ionic flux distribution increases with magnetic field strength and the radial distance corresponding to maximum ionic flux is insensitive to magnetic field strength. Similarly, **Fig. 10b** shows how the deposition flux profiles on the substrate increases with the magnetic field strength B = {0.15, 0.20, 0.25, 0.30} T. Here, the substrate radius and substrate-target distance are set to be equal to the target radius. The geometry, pressure and temperature of the chamber (**Fig. 3**) remain unchanged. In DC magnetron, the presence of magnetic field helps stabilize discharge under low-pressure conditions. With increasing magnetic field strength, the discharge electron density intensifies leading to increased Ar^+ flux on the target and therefore, increased deposition flux of sputtered atoms on the substrate.

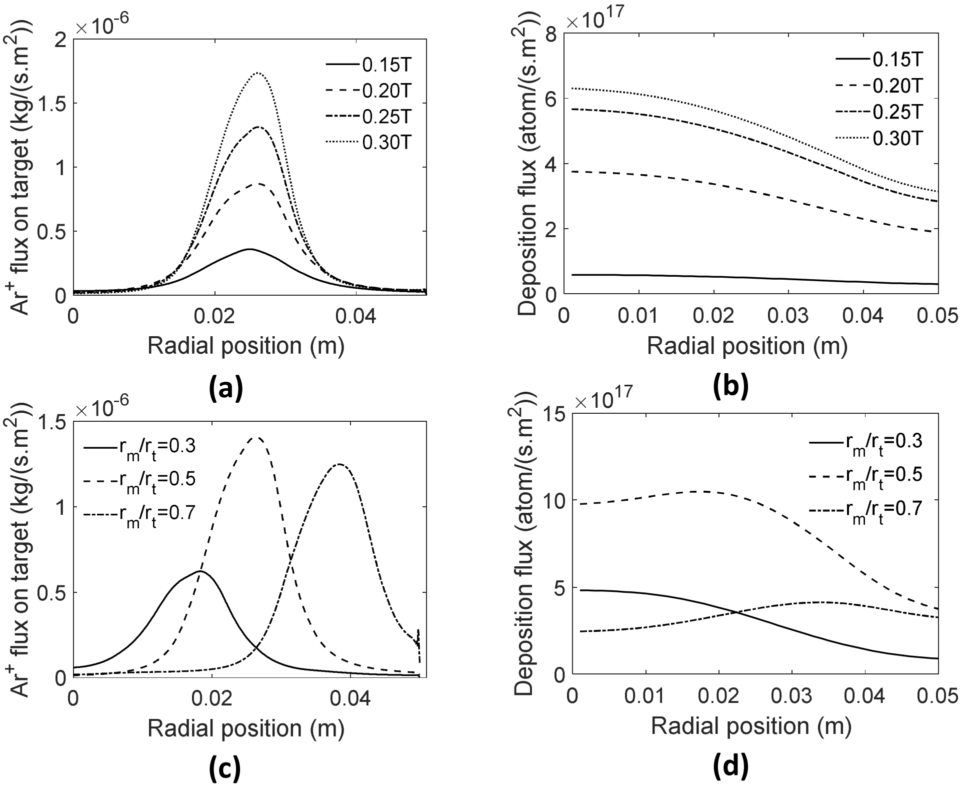

Fig. 10. (a) Ar^+ ionic flux profile on the target and (b) deposition flux of Al and Sc atoms depend on magnet field strength B = {0.15, 0.20, 0.25, 0.30} T with relative position of the magnet $r_m/r_t = 0.5$. (c) Ar^+ ionic flux profile on the target and (d) deposition flux of Al and Sc atoms depend on relative position of the magnet r_m/r_t = {0.3, 0.5, 0.7} for magnet field strength B = 0.25 T.

Fig. 10c shows how the Ar^+ ionic flux profile on the target surface depends on the relative position of the magnet, whose normalized radial distance r_m/r_t = {0.3, 0.5, 0.7}. Here, the substrate radius is set to be same as target radius and substrate-target distance is chosen to be one-half of target radius. It is observed that the position of the magnet affects the ionic flux distribution non-linearly, notably, the peak ionic flux occurs at intermediate $r_m/r_t = 0.5$. This may be due to the optimal balance of increasing magnetic strength with increasing radial distance of magnet, and the coupling with the electric fields between target and substrate so that if the magnet falls outside the edge of target, the effect of electron focusing will be reduced. Hence, there exists an optimum location for magnets so that the maximum Ar^+ ionic flux could be achieved.

Fig. 10d shows the deposition flux on substrate depends on the relative position of the magnet. The ionic flux on target strongly affects the deposition flux curve on the substrate. Strong influence of erosive target pattern on the film thickness shape is also observed when the target-substrate distance is small [32]. As before, the peak deposition flux is at maximum for r_m/r_t = 0.5. In terms of compositions, we observe very minor effect due to the magnetic field strength or position of the magnet. The Sc content in thin films is found to be 37.67 % and 37.87 % for B = 0.5 T and 1.5 T, respectively.

3.2.3. Substrate radius and substrate-target distance

Fig. 11a shows the deposition flux of Al and Sc atoms on the substrate as a function of normalized radial distance r/r_t varying substrate radii r_s/r_t = {0.5, 1.0, 1.5}, where r_t is target radius. Here the substrate-target distance is set as target radius d = r_t. We observe that film thickness is more uniform for smaller substrate radius and the deposition flux is higher near the center. **Fig. 11b** shows the effect of varying normalized target-substrate distance d/r_t = {0.5, 1.0, 1.5} on deposition flux. Here the substrate radius is set as target radius r_s = r_t. We observe that the deposition flux increases with decreasing substrate-target distances due to increased deposition efficiency and reduced scattering losses. For a short gap d/r_t = 0.5, most of sputtered atoms deposit normally onto the substrate leading to characteristic racetrack profile. For increased target-substrate distance, the frequency of collision between sputtered atoms and background gas increases resulting in radial dispersion. As a result, the deposition flux decreases, and the resultant thin film is more uniform.

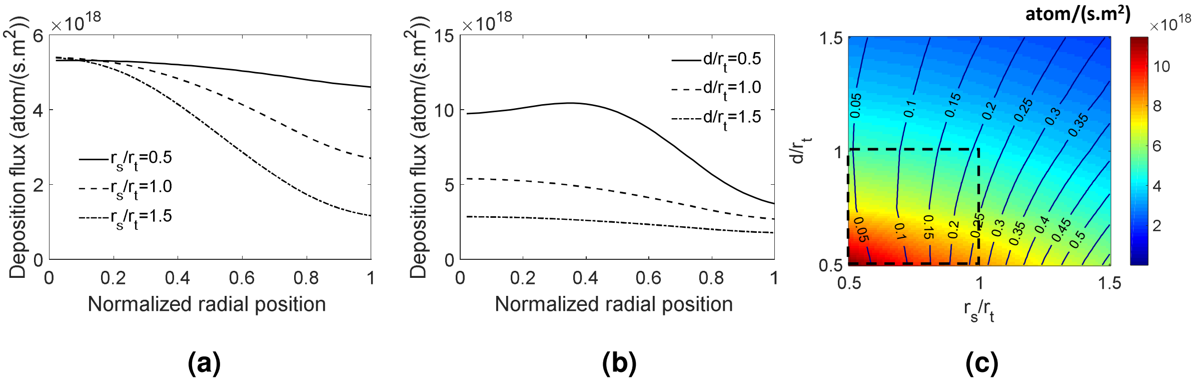

Fig. 11. Deposition flux of Al and Sc atoms onto the substrate as a function of normalized radial distance r/r_t, varying (a) normalized substrate radius r_s/r_t where target-substrate distance equals target radius $d=r_t$, (b) normalized substrate-target distance d/r_t where substrate radius equals target radius $r_s=r_t$, and (c) contour of normalized standard deviation of film

thickness and parametric color map of average deposition flux (in atom/(s.m^2)) of sputtered Al, Sc atoms on the thin film, depending on normalized target-substrate distance and substrate radius.

For clarity, we plot the contour of normalized standard deviation of thin film thickness and parametric color map of average deposition flux (atom/(s.m^2)) depending on normalized target-substrate distance and substrate radius as shown in **Fig. 11c**. Because the film thickness is proportional to the deposition flux, its normalized standard deviation can be approximated from the deposition flux along the substrate radius. Here, the normalized standard deviation of thin film thickness which characterizes the surface uniformity of thin film is defined as

$$\delta = \sqrt{\frac{\sum(x_i/\mu - 1)^2}{N}} \tag{3}$$

where

N is the number of sample points on substrate radius

x_i is the deposition flux at sample point

μ is the mean value of deposition flux along substrate radius

Fig. 11c shows that (1) the film thickness is more uniform for smaller substrates $r_s/r_t < 1$ and (2) the deposition flux is greater for shorter target-substrate distances $d/r_t < 1$, consistent with literature findings [32, 38, 39]. Combining these results, we infer that an optimal design that aims to maximize both high deposition flux and consistent thin film uniformity would confine the relevant geometric parameters within the respective indicated limits, i.e. $r_s/r_t < 1$ and $d/r_t < 1$.

Based on apparent topographical gradients (**Fig. 11c**), our results show that the uniformity of substrate film thickness is affected more strongly by substrate size ratio r_s/r_t compared to target-substrate distance d/r_t. Conversely, the deposition flux appears to be affected more strongly by target-substrate distance d/r_t compared to substrate size ratio r_s/r_t. This suggests that desired characteristics of substrate uniformity and deposition flux can be decoupled and optimized independently through geometric means.

Separately, we found that the composition of the deposited thin film is insensitive to substrate size, whereas the substrate-target distances could affect the substrate composition due to transport losses. Specifically, the Sc content (percentage by number of atoms) in thin films are found to be 37.1% and 38.5% between target-substrate distances of d/r_t = 0.5 and 1.5, respectively.

4. Conclusions

In this study, we propose a numerical framework for multi-scale, multi-physics modeling planar DC magnetron sputtering. Heat transfer and fluid flow processes are solved by LBM, DC magnetron discharge transport by FEM, sputtering and the transportation of atoms from target to substrate process by binary collision approximation Monte-Carlo method.

To improve operational and chamber designs, we conduct parametric studies to investigate the effects of geometry, discharge and chamber working condition on thin film uniformity, deposition flux and composition. We found that reduced substrate radius and substrate-target distance can lead to improved deposition efficiency and film uniformity. Our results also show that magnetic fields can significantly affects the substrate deposition flux and film uniformity but do not directly impact the composition of the film. Instead, the Sc content in the substrate is found to scale linearly with chamber pressure and inverse temperature, although the effect of temperature is considerably marginal under low pressure conditions.

Our present work distinguishes itself from other sputtering studies, such as [40], in that we estimated the incident argon ion flux through magnetron DC plasma simulation and the sputtering yield on the target as a spatial distribution, leading to racetrack pattern.

In summary, magnetron sputtering is powerful technique for thin film deposition coupling electromagnetics, fluid dynamics, discharge chemistry and thermal transport across length scales. Much insight can be obtained through multi-physical modeling and simulation of transport processes, leading to improved operational heuristics. Future work includes reactive gas sputtering and non-homogeneous targets and substrates.

Data availability statement

The data that support the findings of this study are available upon request from the authors.

Acknowledgement

We would like to thank the UGent team for the easy access to SIMTRA and their support in setting-up the code. We also thank Dr. Andreas Mutzke (Max Planck Institute for Plasma Physics, Germany) for sharing SDTrimSP software. This work is supported by A*STAR Programmatic Funds (AME) under the project "Ferroelectric Aluminum Scandium Nitride (Al1-xScxN) Thin Films and Devices for mm-Wave and Edge Computing" (Grant ID: A20G9b0135).

References

[1] J.E. Greene, Review article: tracing the recorded history of thin-film sputter deposition: from the 1800s to 2017, J. Vac. Sci. Technol. A 35 (2017) 05C204.
[2] P.J. Kelly, R.D. Arnell, Magnetron sputtering: a review of recent developments and applications, Vacuum 56 (2000) 159-172.
[3] R. Behrisch, W. Eckstein, Sputtering by Particle Bombardment: Experiments and Computer Calculations from Threshold to MeV Energies, Springer, Berlin, 2007.
[4] P.M. Martin, Handbook of Deposition Technologies for Films and Coatings : Science, Applications and Technology, William Andrew, Oxford, 2010.
[5] G. Bräuer, B. Szyszka, M. Vergöhl, R. Bandorf, Magnetron sputtering – milestones of 30 years, Vacuum 84 (2010) 1354-1359.
[6] R.K. Waits, Planar magnetron sputtering, J. Vac. Sci. Technol. 15 (1978) 179.
[7] I. Kolev, A. Bogaerts, Numerical models of the planar magnetron glow discharges, Contrib. to Plasma Phys. 44 (2004) 582-588.
[8] I. Kolev, A. Bogaerts, PIC – MCC Numerical Simulation of a DC Planar Magnetron, Plasma Processes and Polymers 3(2) (2006) 127-134.
[9] T. Yagisawa, T. Makabe, Modeling of dc magnetron plasma for sputtering: Transport of sputtered copper atoms, J. Vac. Sci. Technol. A 24 (2006) 908.
[10] C. Costin, L. Marques, G. Popa, G. Gousset, Two-dimensional fluid approach to the dc magnetron discharge, Plasma Sources Sci. Technol. 14 (2005) 168-176.
[11] L. Xie, P. Brault, J.-M. Bauchire, A.-L. Thomann, L. Bedra, Molecular dynamics simulations of clusters and thin film growth in the context of plasma sputtering deposition, J. Phys. D: Appl. Phys. 47 (2014) 224004.
[12] P. Brault, SothearaChuon, Jean-MarcBauchire, Molecular dynamics simulations of platinum plasma sputtering: a comparative case study, Front. Phys. 4 (2016) 20.
[13] G. Zhu, J. Sun, L. Zhang, Z. Gan, Molecular dynamics simulation of temperature effects on deposition of Cu film on Si by magnetron sputtering, J. Cryst. Growth 492 (2018) 60-66.
[14] L. Zhang, S. Tian, T. Peng, Molecular simulations of sputtering preparation and transformation of surface properties of Au/Cu alloy coatings under different incident energies, Metals 9 (2019) 259.
[15] L.R. Shaginyan, M. Misina, S. Kadlec, L. Jastrabık, A. Mackova, V. Perina, Mechanism of the film composition formation during magnetron sputtering of WTi, J. Vac. Sci. Technol. A 19 (2001) 2554-2566.
[16] J. Ziegler, J.P. Biersack, M.D. Ziegler, SRIM-The Stopping and Ranges of Ions in Solids, SRIM Co., Chester, www.srim.org, (2008).
[17] H. Hofsäss, K. Zhang, A. Mutzke, Simulation of ion beam sputtering with SDTrimSP, TRIDYN and SRIM, Appl. Surf. Sci. 310 (2014) 134-141.
[18] A. Mutzke, W. Eckstein, Ion fluence dependence of the Si sputtering yield by noble gas ion bombardment, Nucl. Instrum. Methods Phys. Res. B 266 (2008) 872-876.

[19] A. Rai, A. Mutzke, R. Schneider, Modeling of chemical erosion of graphite due to hydrogen by inclusion of chemical reactions in SDTrimSP, Nucl. Instrum. Methods Phys. Res. B 268 (2010) 2639-2648.
[20] K.V. Aeken, S. Mahieu, D. Depla, The metal flux from a rotating cylindrical magnetron: a Monte Carlo simulation, J. Phys. D: Appl. Phys 41 (2008) 205307.
[21] D. Depla, W.P. Leroy, Magnetron sputter deposition as visualized by Monte Carlo modeling, Thin Solid Films 520 (2012) 6337-6354.
[22] J.-O. Achenbach, S. Mráz, D. Primetzhofer, J.M. Schneider, Correlative experimental and theoretical investigation of the angle-resolved composition evolution of thin films sputtered from a compound Mo_2BC target, Coatings 9 (2019) 206.
[23] P. Mareš, J. Vlček, J. Houška, J. Kohout, J. Čapek, Effect of energetic particles on pulsed magnetron sputtering of hard nanocrystalline MBCN (M = Ti, Zr, Hf) films with high electrical conductivity, Thin Solid Films 688 (2019) 137334.
[24] K. Strijckmans, D. Depla, Modeling target erosion during reactive sputtering, Appl. Surf. Sci. 331 (2015) 185-192.
[25] J. Rezek, T. Kozák, N. Kumar, S. Haviar, Synergy of experiment and model for reactive HiPIMS: effect of discharge parameters on WOx composition and deposition rate, J. Phys. D: Appl. Phys. 54 (2021) 125202.
[26] N. Jeong, Lattice Boltzmann approach for the simulation of rarefied gas flow in the slip flow regime, J. Mech. Sci. Technol. 27 (2013) 1753-1761.
[27] L. Wang, Z. Guo, C. Zheng, Multi-relaxation-time lattice Boltzmann model for axisymmetric flows, Comput. Fluids 39(9) (2010) 1542-1548.
[28] L. Zheng, B. Shi, Z. Guo, C. Zheng, Lattice Boltzmann equation for axisymmetric thermal flows, Comput. Fluids 39(6) (2010) 945-952.
[29] C. Costin, T.M. Minea, G. Popa, G. Gousset, Fluid modelling of DC magnetrons-low pressure extension and experimental validation, Plasma Process. Polym. 4 (2007) S960-S964.
[30] Comsol Multiphysics 5.6, Plasma module user's guide.
[31] A. Farhadizadeh, T. Kozák, The importance of discharge voltage in DC magnetron sputtering for energy of sputtered and backscattered atoms on the substrate: Monte-Carlo simulations, Vacuum 196 (2022) 110716.
[32] S. Swann, Film thickness distribution in magnetron sputtering, Vacuum 38 (1988) 791-794.
[33] J. Schmitz, A. Mutzke, A. Litnovsky, F. Klein, X.Y. Tan, T. Wegener, P. Hansen, N. Aghdassi, A. Eksaeva, M. Rasinski, A. Kreter, J. Gonzalez-Julian, J.W. Coenen, C. Linsmeier, M. Bram, Preferential sputtering induced Cr-Diffusion during plasma exposure of WCrY smart alloys, Journal of Nuclear Materials 526 (2019) 151767.
[34] M.W. Thompson, Atomic collision cascades in solids, Vacuum 66 (2002) 99-114.
[35] Y.-Y. Chen, S.-B. Hung, C.-J. Wang, W.-C. Wei, J.-W. Lee, High temperature electrical properties and oxidation resistance of V-Nb-Mo-Ta-W high entropy alloy thin films, Surf. Coat. Technol. 375 (2019) 854-863.
[36] H. Schwarz, T. Uhlig, N. Rösch, T. Lindner, F. Ganss, O. Hellwig, T. Lampke, G. Wagner, T. Seyller, CoCrFeNi high-entropy alloy thin films synthesised by magnetron sputter deposition from spark plasma sintered targets, Coatings 11 (2021) 468.
[37] A.M. Myers, J.R. Doyle, Monte Carlo simulations of sputter atom transport in low-pressure sputtering: The effects of interaction potential, sputter distribution, and system geometry, J. Appl. Phys. 72 (1992) 3064.
[38] D. Golosov, S. Melnikov, S. Zavadski, V. Kolos, J. Okojie, The increase in thickness uniformity of films obtained by magnetron sputtering with rotating substrate, Plasma Sci. Technol. 3 (2016) 100-104.
[39] B. Wang, X. Fu, S. Song, H.O. Chu, D. Gibson, C. Li, Y. Shi, Z. Wu, Simulation and optimization of film thickness uniformity in physical vapor deposition, Coatings 8 (2018) 325.
[40] E. Särhammar, E. Strandberg, N. Martin, T. Nyberg, Int. J. Mater. Sci. Appl. 3 (2014) 29-36.

[41] I. Rafatov, D. Akbar, S. Bilikmen, Modelling of non-uniform DC driven glow discharge in argon gas, Phys. Letts. A 367 (2007) 114-119.
[42] I. Rafatov, E.A. Bogdanov, A.A. Kudryavtsev, On the accuracy and reliability of different fluid models of the direct current glow discharge, Phys. Plasmas 19 (2012) 033502

Appendix A: Governing equations

The governing equations of magnetron DC plasma for the fluid model comprised of four species: electron (e), argon ion (Ar^{+}), excited argon (Ar^{*}) and neutral argon (Ar) [31], as follows:

1. Transport equations for electron density are

$$\frac{\partial}{\partial t}(n_e) + \nabla\cdot\mathbf{\Gamma}_e = R_e - (\boldsymbol{u}.\nabla)n_e, \tag{1}$$

$$\mathbf{\Gamma}_e = -n_e(\boldsymbol{\mu}_e\cdot\boldsymbol{E}) - \boldsymbol{D}_e\nabla n_e. \tag{1a}$$

2. Transport equations for electron energy density are

$$\frac{\partial}{\partial t}(n_\varepsilon) + \nabla\cdot\mathbf{\Gamma}_\varepsilon + \boldsymbol{E}\cdot\mathbf{\Gamma}_e = R_\varepsilon - (\boldsymbol{u}.\nabla)n_\varepsilon, \tag{2}$$

$$\mathbf{\Gamma}_\varepsilon = -n_\varepsilon(\boldsymbol{\mu}_\varepsilon\cdot\boldsymbol{E}) - \boldsymbol{D}_\varepsilon\nabla n_\varepsilon. \tag{2a}$$

3. Transport equations for Argon ion density are

$$\frac{\partial}{\partial t}(n_i) + \nabla\cdot\mathbf{\Gamma}_i = R_i - (\boldsymbol{u}.\nabla)n_i, \tag{3}$$

$$\mathbf{\Gamma}_i = -n_i(\boldsymbol{\mu}_i\cdot\boldsymbol{E}) - \boldsymbol{D}_i\nabla n_i. \tag{3a}$$

4. Transport equations for uncharged species densities (excited and neutral argons) are

$$\frac{\partial}{\partial t}(n_m) - \boldsymbol{D}_m\cdot\nabla^2 n_m = R_m - (\boldsymbol{u}.\nabla)n_m. \tag{4}$$

5. Electromagnetic equations (Maxwell's equations) are

$$\nabla^2 V = -\frac{\rho_v}{\varepsilon_0\varepsilon_r}, \tag{5}$$

$$\rho_v = e(n_i - n_e), \tag{5a}$$

$$\boldsymbol{E} = -\nabla V. \tag{5b}$$

The auxiliary equations are as follows. The electron and argon ion density source terms are

$$R_{e,i} = \sum_{j=1}^{M} k_j n_j n_e. \tag{6}$$

The electron energy density source term is

$$R_\varepsilon = \sum_{j=1}^{M} k_j n_j n_\varepsilon \Delta E_j. \quad (7)$$

The plasma reaction rates are

$$k_j = \gamma \int_0^\infty \varepsilon \sigma_j(\varepsilon) f(\varepsilon) d\varepsilon. \quad (8)$$

The electron energy distribution function (Maxwellian) is

$$f(\varepsilon) = \bar{\varepsilon}^{(-3/2)} \beta_1 exp(-\varepsilon \beta_2 / \bar{\varepsilon}). \quad (9)$$

Where $\boldsymbol{u}$ refers to the gas flow velocity. The electron mobilities $\boldsymbol{\mu}_e, \boldsymbol{\mu}_i, \boldsymbol{\mu}_\varepsilon$ refer to electron, argon ion and energy respectively, expressed as [41]

$$\boldsymbol{\mu}_e^{-\mathbf{1}} = \begin{bmatrix} \frac{1}{\mu_{dc}} & -B_z & B_y \\ B_z & \frac{1}{\mu_{dc}} & -B_x \\ -B_y & B_x & \frac{1}{\mu_{dc}} \end{bmatrix}, \quad (10a)$$

$$\boldsymbol{\mu}_i = \frac{4.411 \times 10^{19}}{\left[1 + \left(7.721 \times 10^{-3} (\boldsymbol{E}/N_m)\right)^{1.5}\right]^{0.33} N_m} \ [cm^2 V^{-1} s^{-1}], \quad (10b)$$

$$\boldsymbol{\mu}_\varepsilon = \left(\frac{5}{3}\right) \boldsymbol{\mu}_e, \quad (10c)$$

where $n_e, n_i, n_\varepsilon, n_m$ are the electron, ion, electron energy and uncharged species densities.

$\boldsymbol{D}_e, \boldsymbol{D}_i, \boldsymbol{D}_\varepsilon, \boldsymbol{D}_m$ are the electron, ion, electron energy and uncharged species diffusivities.

$$\boldsymbol{D}_e = \boldsymbol{\mu}_e T_e, \quad (11a)$$

$$\boldsymbol{D}_i = \boldsymbol{\mu}_i T_i, \quad (11b)$$

$$\boldsymbol{D}_\varepsilon = \boldsymbol{\mu}_\varepsilon T_e. \quad (11c)$$

T_e and T_i are the electron and ion temperatures, where $T_e = 2/3\,(n_\varepsilon / n_e)$.

Nomenclature

$\varepsilon, \bar{\varepsilon}$ are individual and mean electron energies.

β_1, β_2 are the constants.

n_j is the density of species participating the reaction j.

ΔE_j is the energy lost in the reaction j.

σ_j is the collision cross section of reaction j.

N_m is the density of neutral Argon.

ε_0 is the permittivity of vacuum.

ε_r is the dielectric constant of Argon.

μ_{dc} is the electron mobility without the present of magnetic field.

B_x, B_y, B_z are the components of external magnetic field in x, y, z directions.

M is the number of reactions.

The elementary reactions for Argon considered in this study are shown in **Table A1**. The cross-sections of these reactions [42] is shown in Fig. A1.

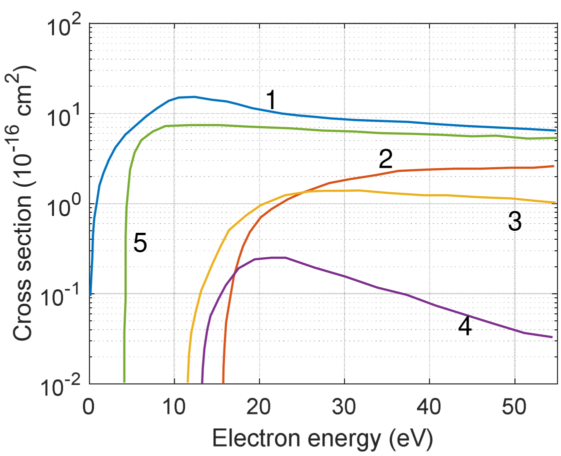

Fig. A1. Electron cross sections for plasma reactions used in the model. Curve labels correspond to indices of corresponding processes in Table A1.

Table A1

Elementary plasma reactions for Argon.

Index	Reaction	Type	ΔE (eV)	Constant
1	$e + Ar \rightarrow e + Ar$	Elastic collision	0	

2	$e + Ar \rightarrow 2e + Ar^{+}$	Direct ionization	15.8	
3	$e + Ar \rightarrow e + Ar^{*}$	Excitation	11.4	
4	$e + Ar \rightarrow e + Ar$	Excitation	13.1	
5	$e + Ar^{*} \rightarrow 2e + Ar^{+}$	Stepwise ionization	4.4	
6	$2Ar^{*} \rightarrow e + Ar^{*} + Ar^{+}$	Penning ionization		$6.2\text{x}10^{-10}\text{cm}^{3}\text{s}^{-1}$
7	$Ar^{*} \rightarrow hv + Ar$	Radiation		$1.0\text{x}107\text{s}^{-1}$

Appendix B: Electromagnetic field and ion flux

Fig. B1 shows the spatial components of discharge electric and magnetic fields in cylindrical coordinates (r,z) in the chamber, revealing large gradients near mid-radius of the target disc focused by magnets. Accordingly, charged particle tracking simulations also show high energy Argon ion bombardment near mid-radius of the target (**Fig. B2**).

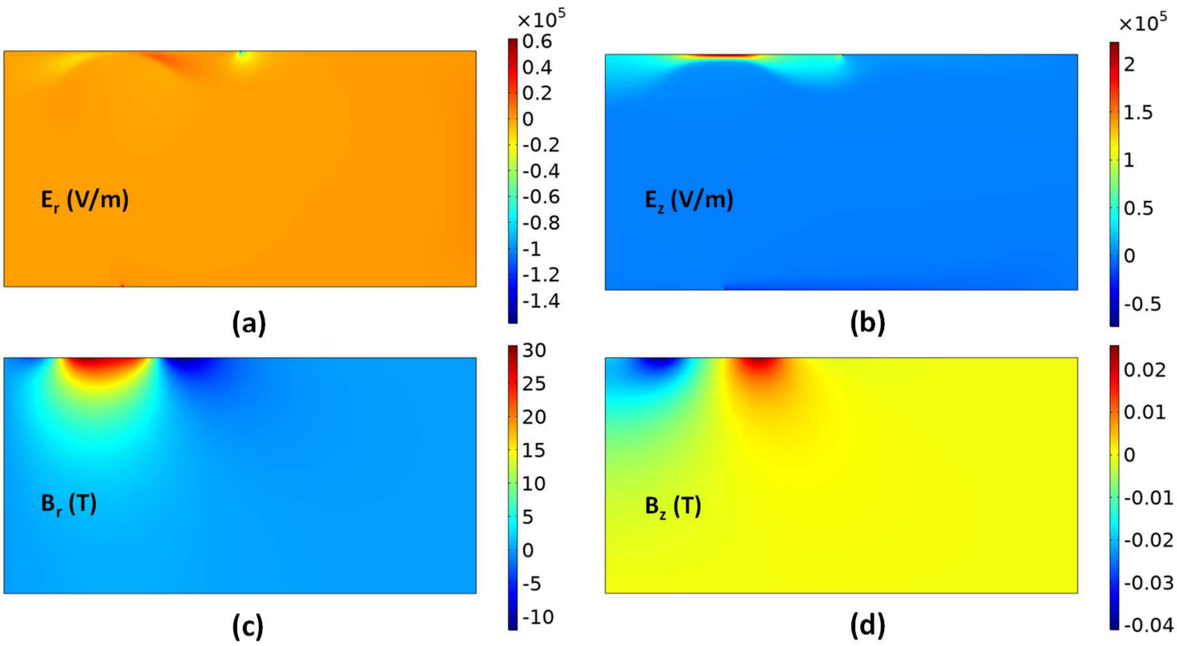

Fig. B1. Electric field in (a) radial and (b) axial directions. Magnetic field in (c) radial and (d) axial directions.

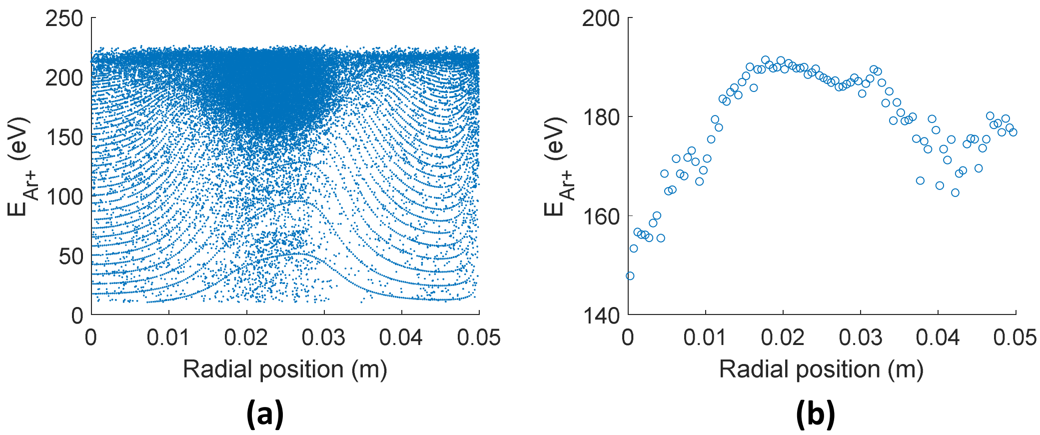

Fig. B2. (a) Scatter (dot) and contour (line) plot of energy of bombarding argon ions on the target. (b) Average energy of bombarding argon ions on the target.